Earth and Planetary Science Letters 299 (2010) 180–189

Contents lists available at ScienceDirect

Earth and Planetary Science Letters

journal homepage: www.elsevier.com/locate/epsl

Fluid-driven fractures in uncemented sediments: Underlying particle-level processes

Hosung Shin [a,*], J. Carlos Santamarina [b]

[a] School of Civil and Environmental Engineering, University of Ulsan, Ulsan, Republic of Korea, 680-749
[b] School of Civil and Environmental Engineering, Georgia Institute of Technology, Atlanta, GA, USA, 30332

A R T I C L E I N F O

Article history:
Received 4 September 2009
Received in revised form 14 August 2010
Accepted 31 August 2010
Available online 28 September 2010

Editor: L. Stixrude

Keywords:
hydraulic fracture
localization
sediments
enhanced oil recovery
CO_2 sequestration
waste disposal

A B S T R A C T

Granular materials subjected to fluid flow may experience fracture formation and fluid flow localization. Current explanations for hydraulic fracture in soils fail to satisfy the inherent characteristics of granular materials: effective stress-dependent cohesionless-frictional strength. We apply complementary experimental and numerical techniques to identify the underlying particle-scale mechanisms. First, we show that the miscibility of the invading fluid with the host fluid leads to distinct localization processes that depend on the balance between particle-level skeletal forces (effective stress-dependent), capillary forces (the invasion of the interfacial membrane when immiscible fluids are involved), and seepage drag forces (associated with fluid flow velocity). Then, we identify the positive feedback mechanisms at surface defects and fracture tips that promote fracture initiation and sustain fracture propagation. These include increased porosity at the tip due to strains preferentially normal to the fracture alignment, either eased membrane invasion (immiscible fluids) or higher hydraulic conductivity (miscible fluids), and the emergence of particle-level forces that promote opening-mode particle displacement. This effective stress compatible sequence of events helps identify the parameters that govern fluid-driven fracture formation in uncemented sediments, and explain experimental observations.

1. Introduction

Hydraulic fractures affect a wide range of geosystems, may cause the failure of man-made structures (Leonards and Davidson, 1984; Sherard, 1986), define the 'geo-plumbing' responsible for the development of oil and gas reservoirs (Brown et al., 1994), enhance resource recovery from C-fuels and geothermal reservoirs (Economides and Nolte, 2000; Nemat-Nasser et al., 1982), facilitate waste injection (Keck and Withers, 1994), and hinder the long-term storage of CO_2 (Cailly et al., 2005; Chalbaud et al., 2009).

Fluid-driven fracture initiation and propagation in brittle solids are dominated by tensile failure (Hubbert and Willis, 1957). This cannot be the case in unconsolidated/uncemented sediments: contrary to solid materials, uncemented granular materials, both fine and coarse-grained, are already "separated" at the particle-scale and their strength is effective stress-dependent. Hence, soils can carry no tensile stress and the effective stress field must be compressive everywhere.

Yet, hypotheses for fracture initiation in granular materials consider tensile failure (Alfaro and Wong, 2001; Andersen et al., 1994; Bjerrum et al., 1972; Jaworski et al., 1981; Terzaghi et al., 1996; Widjaja et al., 1984), shear failure (Atkinson et al., 1994; Chang, 2004; Komak Panah and Yanagisawa, 1989), or a combined failure mode (Mori and Tamura, 1987; Soga et al., 2006). Shear failure is compatible with a cohesionless-frictional strength envelope, but most hydraulic fractures in soils exhibit opening-mode (e.g. X-ray images in Toshikazu et al., 2002), and the orientation is perpendicular to the minor effective principal stress rather than in the 45° orientation corresponding to shear failure. Predictions based on total stress parameters may match the opening-type failure mode, but they need to assume tensile resistance which cannot be justified in effective stresses. These observations categorically imply that previous hypotheses for hydraulic fracture in uncemented sediments are not compatible with the fundamental behavior of uncemented granular materials.

The purpose of this study is to identify effective stress compatible mechanisms for fracture formation and propagation in unconsolidated/uncemented sediments caused by the forced invasion of either immiscible or miscible fluids. We report the results of a unique experimental study designed to identify particle-level mechanisms. Then, we explore the macro-scale evolutions of effective stress and void ratio with time.

2. Experimental study

The initiation of hydraulic fractures on planar sediment surfaces (instead of boreholes) is experimentally studied using the cylindrical stainless steel cell shown in Table 1a. A Ca-montmorillonite slurry (liquid limit = 97%, plastic limit = 47%, initial water content w = 150%) is placed inside the chamber and allowed to consolidate

* Corresponding author.
E-mail address: shingeo@ulsan.ac.kr (H. Shin).

0012-821X/$ – see front matter © 2010 Elsevier B.V. All rights reserved.
doi:10.1016/j.epsl.2010.08.033

Table 1
Methodology. a) Experiments. b) Numerical analysis.

a) Experimental device

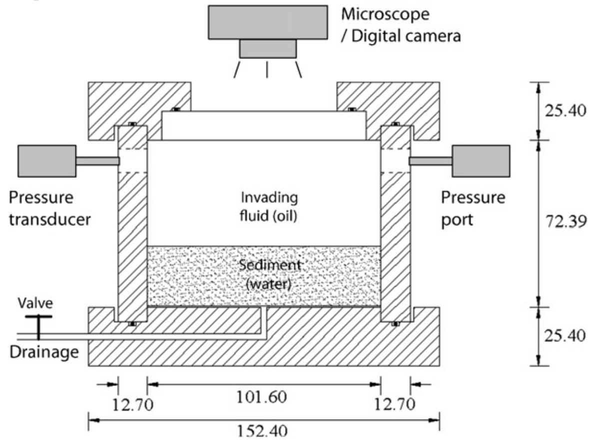

Cylindrical, stainless steel chamber see-through window built in the top cap
Note: all dimensions in [mm]

b) Numerical simulation

b-1. Element type and boundary conditions

Results in Figures 4 and 5

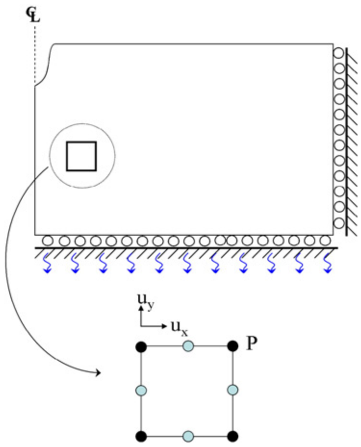

Element type: 4 nodes for fluid pressure and 8 nodes for displacement. 2D plane strain. No friction against boundaries.

Results in Figure 6

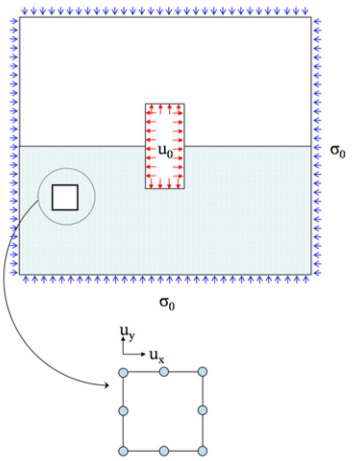

Element type: 8 nodes for displacement. 2D plane strain. Constant σ′ on the boundary, u_0 around the notch surface.

Results in Figure 8

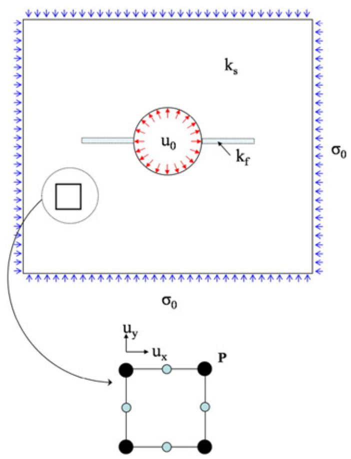

Element type: 4 nodes for fluid pressure and 8 nodes for displacement. 2D plane strain. Constant σ′ on the boundary, u_0 around the borehole.

b-2. Model and material properties

Constitutive model: Modified Cam clay model. Adopts Hvorslev surface and tension cut-off. Associated flow rule. Soil properties: normally consolidated sediment, compression index $C_c = 0.46$, swelling index $C_s = 0.15$, void ratio at 1 kPa $e_{1\ kPa} = 3$, failure stress ratio $M = 1.2$, drained Poisson's ratio $\nu = 0.3$

to 2 kPa. Then, the chamber is filled with either an immiscible fluid (colorless and transparent safflower oil, viscosity $\mu = 50$ cP) or a miscible fluid (water) that rests on top of the sediment. The supernatant fluid is pressurized to force it to invade the soil mass. The formation of fractures on the soil surface is recorded using high resolution digital photography in time-lapse mode.

Drainage starts immediately after opening the bottom drainage port. At first, the sediment settles evenly. Fractures initiate after a certain time delay and always originate at surface defects such as minute sub-millimeter surface dimples as can be seen in Figure 1. Hence, hydraulic fracturing is intimately linked to pressure diffusion and the triggering effect of surface defects. Closing the bottom drainage port after crack initiation halts propagation when either immiscible or miscible fluids are involved. This implies that the driving force for fracture propagation vanishes in a closed system.

Specimens are analyzed at the end of the test. When an immiscible fluid was forced onto the sediment, we observe no evidence of oil invasion into the sediment except at fractures, and the initially soft sediment had become stiff throughout the whole depth. However, specimens tested with a miscible fluid have remained soft near the top surface but stiffened towards the bottom.

3. Particle-level forces

Grains displace δ as a fracture opens. Displacements $\delta = at^2/2$ are the integral of accelerations 'a' that result from unbalanced particle-level forces, $F = ma$. The most important particle-level forces F [N] in a medium made of grain size d_s [m] being invaded by either a miscible or an immiscible fluid are: the weight of grains $W = \pi d_s^3 \rho g/6$ composed of a mineral with mass density ρ [kg/m3], the skeletal force $F_{sk} = \sigma' d_s^2$ that grains must carry due to the local effective stress σ′ [N/m^2], the capillary force $F_c = \pi d_s T_S$ caused by immiscible fluids with interfacial tension T_S [N/m], and the seepage force $F_s = 3\pi\mu v d_s$ produced by a fluid of viscosity μ [N·sec/m^2] when it traverses pores with flow velocity v [m/s].

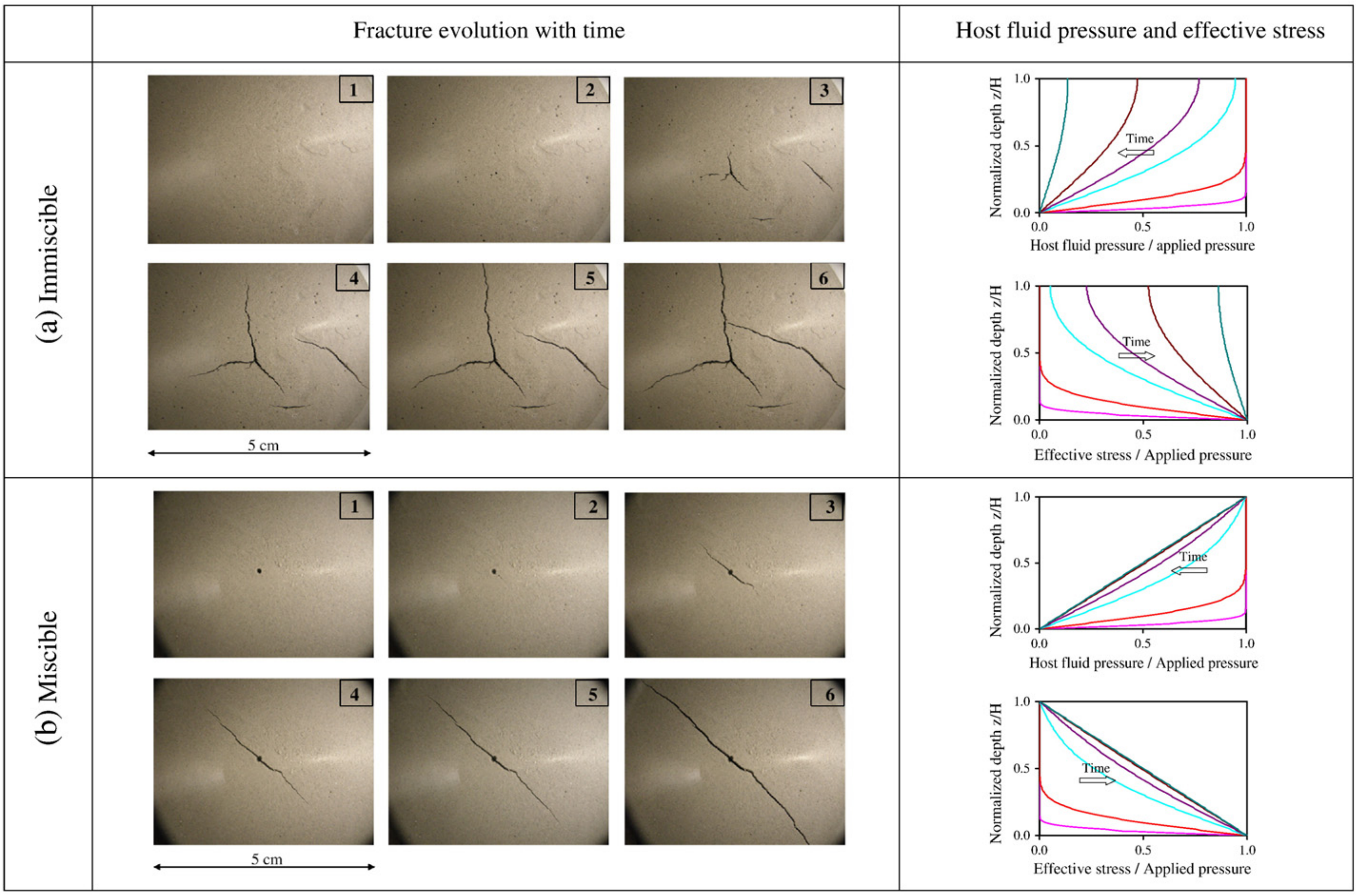

Fig. 1. Hydraulic fracture formation on the soil surface. (a) Immiscible fluid (pressure 200 kPa). (b) Miscible fluid (pressure 350 kPa).

Sketches in Figure 2 show capillary forces (Fig. 2a) and seepage drag forces (Fig. 2b) that are expected during the forced invasion of an immiscible fluid or a miscible fluid. Note that capillary and seepage forces tend to cause (i) particle separation at the tip of a surface defect (or at the tip of a fracture), (ii) grain convergence near the shoulder of the defect, and (iii) 1D compaction in the far field.

An opening will form in the soil mass when capillary and/or seepage forces exceed the local skeletal force and the particle self-weight. The relevance of particle size d_s is highlighted by the linear f(d_s), square f(d_s^2) or cubic f(d_s^3) dependency of these forces: weight and skeletal forces decrease faster than capillary and drag forces with decreasing particle size. We note that: (1) high local gradients and pore velocities of the fluid at the fracture tip determine the drag forces, (2) the van der Waals attraction force F_{att} scales with the grain size d_s and remains much smaller than the capillary force for all d_s, $F_{att} \ll F_c$ (not included among governing forces above). Hence, capillary and seepage-related drag forces can overtake self-weight and skeletal forces as particle size decreases, and fine-grained soils are more susceptible to fluid-driven fracture formation.

Typically particle displacements are very small in coarse-grained sediments, and sediments are invaded without experiencing particle separation (capillary and seepage forces are much smaller than skeletal forces-zone “a” in Fig. 3). Capillary forces gain relevance when an immiscible fluid is forced to invade fine-grained soils and can effectively cause the wedge action that promotes opening-mode fracture propagation (zone “b” in Fig. 3). Hydraulic fracture initiation in granular media driven by miscible fluids requires sufficient drag to open and support the fracture walls (zone “c” in Fig. 3). This can be achieved either in fine-grained soils, using high viscosity fluids, imposing high flow velocity, or promoting filter-cake formation (Khodaverdian and McElfresh, 2000). Finally, seepage and capillary forces may combine to cause fluid-driven localization under mixed conditions (zone “d” in Fig. 3).

4. Numerical analyses

We capture the mechanisms postulated above in finite element simulations to further investigate on the formation of hydraulic fractures driven by the forced invasion of immiscible and miscible fluids in soils. We conduct all studies in effective stresses to explicitly recognize the particulate nature of granular materials. We represent the soil mass using the Modified Cam Clay model, adopt the Hvorslev surface to avoid overestimating the peak shear strength, and assume zero soil cohesion by imposing the tension cut-off boundary (Muir Wood, 1990; Schofield, 1980). Other constitutive model parameters, simulation details and boundary conditions are summarized in Table 1b.

4.1. Immiscible fluid

The interfacial membrane between the two immiscible fluids rests on the sediment surface and acts as an impermeable boundary. The pressure u_{inv} is applied normal to the top boundary and drainage is allowed through the bottom of the specimen (Table 1b).

Numerical results are shown in Figure 4 for a given geometry of the surface defect at dimensionless time $T = t/(H^2/c_v) = 0.33$ where H is the sediment thickness. Away from the surface defect, strains are vertical and void ratio changes follow the 1D normal consolidation line everywhere in the far field (~k_0-“iii” in Figure 4—Numerical results agree with analytical predictions shown in Fig. 1a). The void ratio decreases the most around the shoulder of a surface defect due to quasi-isotropic confinement imposed by the interfacial membrane

(~isotropic—"ii" in Fig. 4). Finally, the void ratio at the tip of the surface defect decreases at a much lower rate (may even increase for some tip geometries), remains higher than anywhere else ("i" in Fig. 4), and strains are primarily in the horizontal direction (Fig. 4c). These numerical results are in agreement with the particle-scale mechanisms shown in Figure 2.

Open fracture initiation is predicted when the pressure difference between the invading and host fluids $u_{inv}-u_{host}$ equals maximum pressure difference P_{max} that a sediment can resist against the advancing interfacial membrane. Assuming parallel platy particles of thickness t_s [m] and mean separation distance $\bar{d}$ [m], the value of P_{max} can be estimated using Laplace equation $P_{max}=2T_s/\bar{d}$ for a cylindrical interface of diameter $\bar{d}$, where T_s is the surface tension between the two contacting fluids. This expression can be written in terms of macro-scale sediment parameters, recognizing that the void ratio e (volume of voids/volume of solid) for this parallel plate configuration is $e=\bar{d}/t_s$, and that specific surface S_s [m^2/g] (surface area/mass) is $S_s=2/(\rho\ t_s)$ where ρ [g/cm^3] is the mineral mass density. Then,

$$P_{max} = [u_{inv}-u_{host}]_{max} = \frac{2T_S}{\bar{d}} = \frac{\rho T_S S_S}{e}. \quad (1)$$

For clarity, the receding contact angle is assumed $\theta\approx 0$ in this analysis.

4.2. Miscible fluid

The supernatant miscible fluid is pressurized and drainage is allowed through the bottom port. Seepage drag forces cause particle displacements; these forces and displacements translate into effective stress changes and strains at the macro-scale. In the absence of an interfacial membrane on the soil surface, the host fluid pressure below the soil surface immediately equals the supernatant fluid pressure,

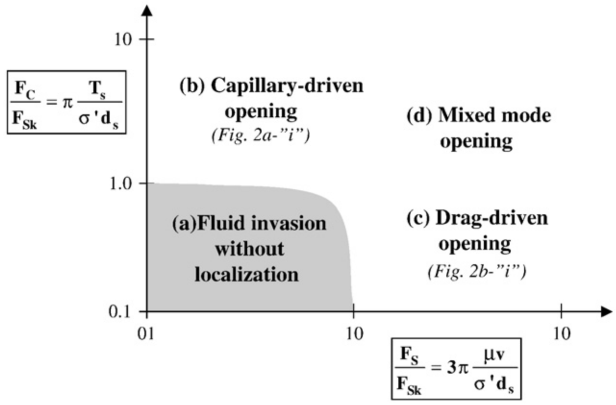

Fig. 3. Hydraulic fracture regimes depending on fluid and soil type. Balance between capillary $F_C=\pi d_s T_S$, skeletal $F_{SK}=\sigma' d_s^2$, and seepage $F_S=3\pi\mu d_s v_f$ forces.

and the effective stress remains null on the soil surface regardless of the applied pressure. This agrees with the very soft sediment condition observed at the end of all tests with miscible fluids. Everywhere else, the imposed gradient i implies a change in effective stress $\Delta\sigma' = \gamma_f \int i ds$, which in-turn causes consolidation (analytical results in Fig. 1b).

Changes in void ratio affect the hydraulic conductivity and flow conditions: clearly, this is an inherently coupled hydro-mechanical problem. Hydraulic conductivity is controlled by pore size and connectivity in the direction of flow (Stewart et al., 2006). Therefore, k cannot be a volume-average isotropic parameter in the context of fracture formation. Various relations have been proposed for stress-dependent (Debschutz et al., 1989; Rice, 1992; Shi and Wang, 1986), and for strain-dependent hydraulic conductivity (Wong, 2003). We prefer a strain-dependent formulation to highlight the inherent link

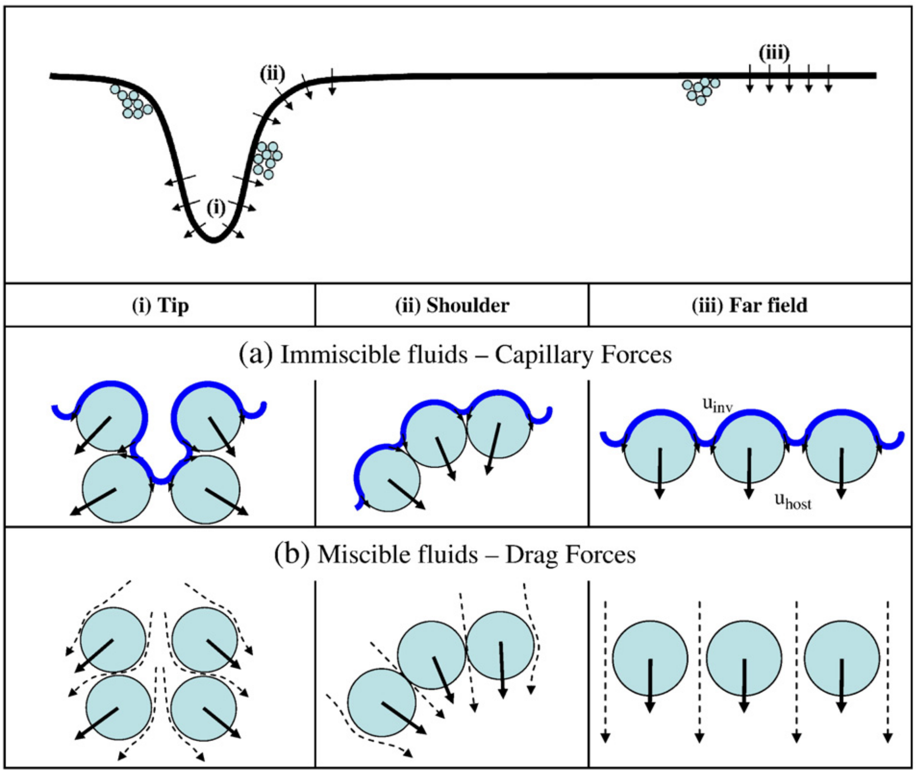

Fig. 2. Particle forces and displacements around a surface defect during the forced invasion of (a) an immiscible fluid, and (b) a miscible fluid.

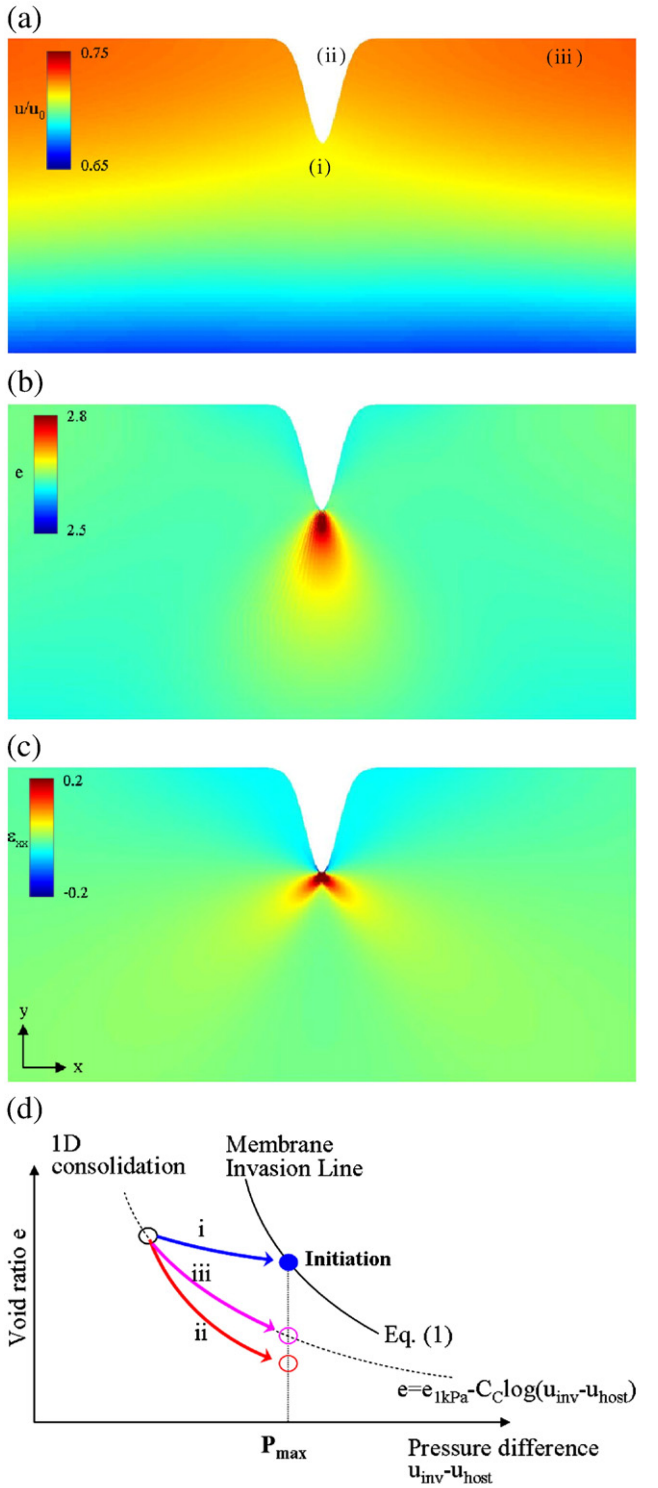

Fig. 4. Numerical simulation of fracture initiation driven by the forced invasion of an immiscible fluid. Results shown at dimensionless time T = 0.33. (a) Pore pressure, (b) Void ratio distributions and (c) Horizontal strain (positive for tensile strain). (d) The evolution of void ratio and pressure difference at the tip (i), shoulder (ii) and in the far field (iii).

between hydraulic conductivity and pore size. The evolution of hydraulic conductivity with strain $k = f(\varepsilon)$ determines the severity of the positive feedback that may eventually lead to run-away fracture formation. The general form of the $k = f(\varepsilon)$ equation we adopt for these simulations reflects the fundamental nature of flow in porous media captured in the Kozeny–Carman equation. Consider a region width w made of N-particles size d_s. A transverse opening width b develops, so that the average strain is $\varepsilon_x = b/w$. Fluid flow is estimated using the Kozeny–Carman equation for the intact material and the Navier–Stokes equation for an incompressible fluid flowing along the opening of width b. Then, the hydraulic conductivity for flow in the y-direction before straining k_{yo} and after straining $k_y(\varepsilon_x)$ are related as:

$$k_y(\varepsilon_x) = \left[1 + 15\frac{1+e}{e^3}N^2\varepsilon_x^3\right]k_{yo} = \left(1 + \lambda\varepsilon_x^3\right)k_{yo} \qquad (2)$$

The second general expression for macro-scale hydraulic conductivity shows sensitivity to the transverse strain ε_x to the third power, amplified by a factor λ which is inversely proportional to the square of the particle diameter. Note the high sensitivity of hydraulic conductivity to tensile strain ε_x perpendicular to the flow direction y, particularly in fine-grained sediments where λ is high. This expression allows us to compute the evolution of the hydraulic conductivity tensor as a function of the strain tensor (computed in the principal strain directions). Then, we rotate hydraulic conductivity tensor to the original coordinates.

Simulation results are presented in Figure 5 at different times after bottom drainage starts. The following observations can be made:

- Seepage normal to the surface in the far field of a surface defect ("iii" in Fig. 2) produces an increase in effective vertical stress; the horizontal stress increases as well according to the k_0 stress ratio at zero lateral strain (Jaky, 1944), and the sediment compacts.
- The presence of the surface defect distorts equi-potential pressure lines and causes the development of a horizontal hydraulic gradient i_x against defect walls and at the tip.
- Strains at the tip of the defect are primarily tensile and horizontal ε_x. Thus, the hydraulic conductivity increases in the vertical direction according to $k_y(\varepsilon_x)$ in Eq. (2). There is almost no change in horizontal hydraulic conductivity.
- A fully fluidized region ($u/u_0 \approx 1$) advances at the tip of the defect indicating open fracture propagation.

These results highlight the role of positive feedback in the coupled hydro-mechanical problem that leads to hydraulic fracture in granular materials.

5. Implications

The previous sections presented experimental, particle-level analyses and corroborating numerical results obtained using an equivalent continuum model consistent with uncemented sediment behavior. Both immiscible and miscible fluid-driven fracture initiation and propagation were analyzed. While there are profound phenomenological differences between miscible and immiscible fluid invasions, the central role of surface defects on fracture initiation is noted in both cases. In this section, we explore related implications.

5.1. Surface defects

Seepage drag or capillary action against a smooth soil surface causes uniform 1D compaction. Similarly, there is uniform cavity expansion in the case of cylindrical or spherical surfaces (Jaworski et al., 1981; Widjaja et al., 1984). In fact, all experimental results show that fluid-driven fracture opening develops when the surface geometry promotes particle forces that favor "hydraulic wedging" and grain separation. In other words, surface defects play a critical role in fracture initiation. Defects include topographic features, existing

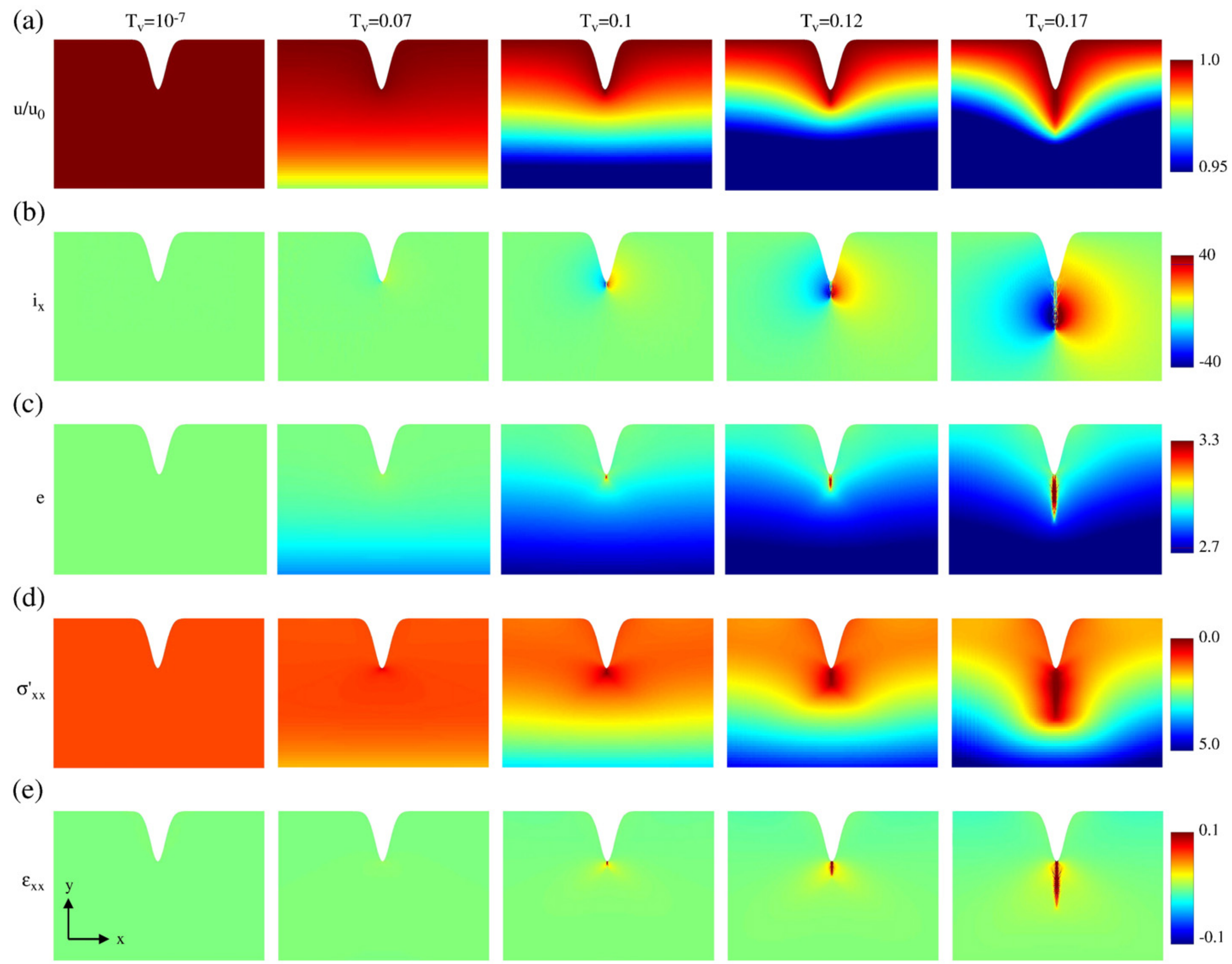

Fig. 5. Hydraulic fracture initiation and propagation from a surface defect driven by the forced invasion of a miscible fluid. Evolution in time of: (a) host fluid pressure normalized by applied pressure u/u_0, (b) horizontal hydraulic gradient i_x, and (c) void ratio e, (d) horizontal effective stress, and (e) horizontal strain (positive for tensile strain).

cracks, heterogeneous stiffness and deformation (Terzaghi et al., 1996; Towner, 1988; Weinberger, 1999). Porosity changes in fine-grained soils can also be due to changes in pore fluid ionic concentration, permittivity or pH (Murray and Quirk, 1990; Palomino and Santamarina, 2005; Wang and Xu, 2007; Zabat et al., 1997).

We investigate the effect of notch geometry on fracture initiation pressure and on the direction of fracture propagation using the numerical approach described above (Numerical model conditions in Table 1b). Results shown in Figure 6 correspond to immiscible fluid invasion of (a) a wide notch, width-to-depth w/L = 0.25, and (b) a narrow notch w/L«1. A high increase in void ratio takes place in the oblique direction at corners of wide notches (Fig. 6a); therefore, initial fracture growth would not be in the notch main direction but at an angle, giving the false impression of a shear failure. This is not the case when slender notches are involved (Fig. 6b): the increase in void ratio is clearly aligned with the direction of the notch prompting fracture propagation along the notch direction.

The scale of surface defects such as dimples and notches is typically much larger than the scale of pores in the sediment. Experimental results show that notches have little or no effect on the fracture initiation pressure *per se*, but on localizing the process (Alfaro and Wong, 2001; de Pater and Dong, 2007; Yanagisawa and Panah, 1994). In other words, the particle-scale defines the pore size for membrane invasion and fluid flow, but the scale and geometry of surface defects are responsible for local changes that favor fracture nucleation.

5.2. Pore size distribution (immiscible fluid)

Eq. (1) predicts the maximum pressure difference P_{max} as a function of the mean pore size d. However, pore size is not uniformly distributed and the interfacial membrane will invade large pores first. Hence, the maximum pressure difference P_{max} will be lower than anticipated by Eq. (1). A better estimate of P_{max} starts by recognizing that most sediments exhibit a log-normal pore size distribution (Garcia-Bengochea et al., 1979; Juang and Holtz, 1986; Li and Zhang, 2009; Tanaka et al., 2003). The standard deviation σ^* in logarithmic scale log(d/μm) is typically between $0.2 \le \sigma^* \le 0.5$ (H. Phadnis—personal communication). The "characteristic pore diameter" d^* on the soil surface that determines massive invasion can be related to the mean pore size by a factor α of the standard deviation $\sigma^*, \log(d^*/\mu m) = \log\left(\overline{d}/\mu m\right) + \alpha\sigma^*$ (Ang and Tang, 1975); then,

$$d^* = \overline{d} \times 10^{\alpha\sigma^*}. \tag{3}$$

The α-factor $\alpha \equiv \left[\log\left(d^*/\overline{d}\right)\right]/\sigma^* \ge 1.0$ determines the percentage of surface pores invaded at P_{max} and is linked to fracture saturation

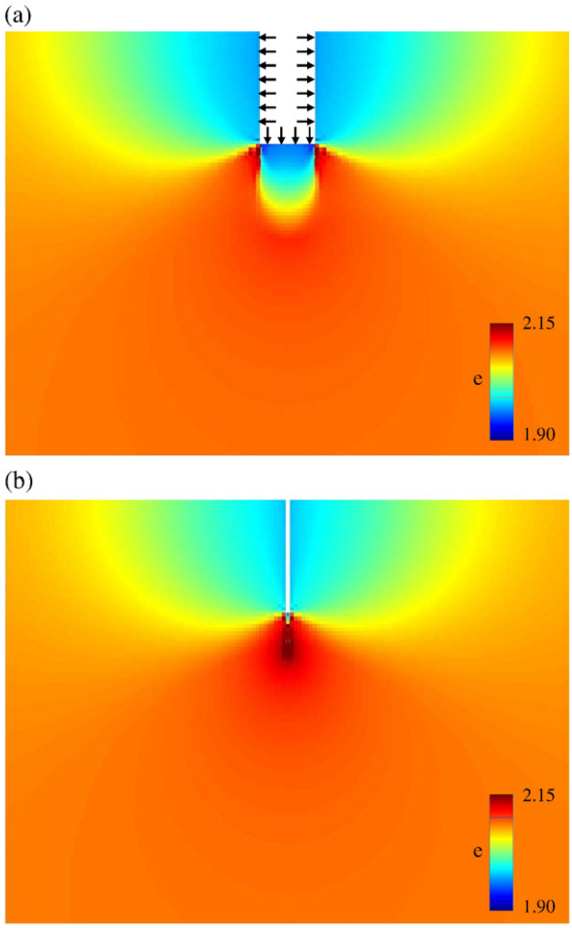

Fig. 6. Numerical simulation for the effect of the notch sharpness on void ratio (Blue = contraction, red = dilation) with immiscible fluid. (a) A wide notch causes an increase in void ratio oblique to the notch alignment. (b) A narrow notch causes void ratio expansion in the direction of the notch. The simulation parameters are applied fluid pressure $u_0 = 200$ kPa, effective confining pressure $\sigma_0 = 100$ kPa.

(Bai et al., 2000). The analysis of limited experimental data on fracture saturation suggests that $\alpha\sigma^*$ ranges between 2 and 3. Combining Eqs. (1) and (3), the statistically modified maximum pressure difference P_{max} becomes

$$P_{\max} = \frac{\rho T_S S_S}{e}\frac{1}{10^{\alpha\sigma*}} \approx \beta\frac{T_S S_S}{e} \quad where\ \beta \sim 10^{-2}\ to\ 10^{-3}. \tag{4}$$

5.3. Initiation time

The fracture initiation time in the test configuration selected for this study is controlled by the rate of pressure diffusion and can be estimated using a 1D diffusion analysis, and the imposed pressure and flow boundary conditions (refer to analytical results in Fig. 1 and numerical evidence in Fig. 5).

5.3.1. Immiscible fluid

The host fluid pressure in the far field of the notch (zone "iii" in Fig. 4) at depth z and time t is computed using the solution of diffusion equation for the boundary conditions $u = 0$ at the lower drainage boundary $z = 0$, and $\partial u/\partial z = 0$ at the "impermeable" soil surface $z = H$ where the interfacial membrane rests (Bardet, 1997),

$$u(Z,T) = \sum_{n=0}^{\infty} \frac{2u_{inv}}{M_n}\sin(M_n Z)\exp\left(-M_n^2 T\right) \tag{5}$$

where u_{inv} is the fluid pressure applied onto the invading immiscible fluid that fills the cell at $z = H$, the parameter M_n is $M_n = \pi(2n+1)/2$, the dimensionless depth is $Z = z/H$, and the dimensionless time is $T = c_v t/H^2$. The interfacial membrane invades the sediment and triggers fracture initiation when the pressure difference on the tip ($z \sim H$) reaches the maximum pressure difference $u_{inv} - u(H,t) = P_{max}$ (Eq. (4)).

Measured fracture initiation times are plotted and compared against the predicted values in Figure 7a. The diffusion coefficient c_v and hydraulic conductivity k are determined from the measured flow rate data. The fracture cannot develop if the applied pressure u_{inv} is lower than P_{max}; in this case, only vertical compaction is observed in the oedometer cell. The fracture initiation time decreases asymptotically as the applied fluid pressure u_{inv} increases.

5.3.2. Miscible fluid

The hydraulic gradient can be estimated by the diffusion equation as well, but in this case the boundary conditions are $u = 0$ at the lower drainage boundary $z = 0$, and $u = u_{inv}$ at the top soil surface $z = H$ (Fig. 5a). The hydraulic gradient at the soil surface $z = H$ in the far field of the notch is,

$$i_y(T) = \frac{u_{inv}}{\gamma_f H}\left(1 + \sum_{n=1}^{\infty} 2\cos(n\pi)\exp\left(-n^2\pi^2 T\right)\right) \tag{6}$$

where γ_f is the fluid unit weight. Numerical simulations show that the horizontal hydraulic gradient $i_x(T)$ at the tip of the surface defects is about 5 times greater than the vertical hydraulic gradient in the far field, i.e. $i_x(T) \approx 5i_y(T)$ for a wedge-shaped notch with width-to-depth ratio 0.1-to-0.5; sharper notches generate slightly higher i_x/i_y ratios. The initial void ratio and sediment stiffness determine the critical

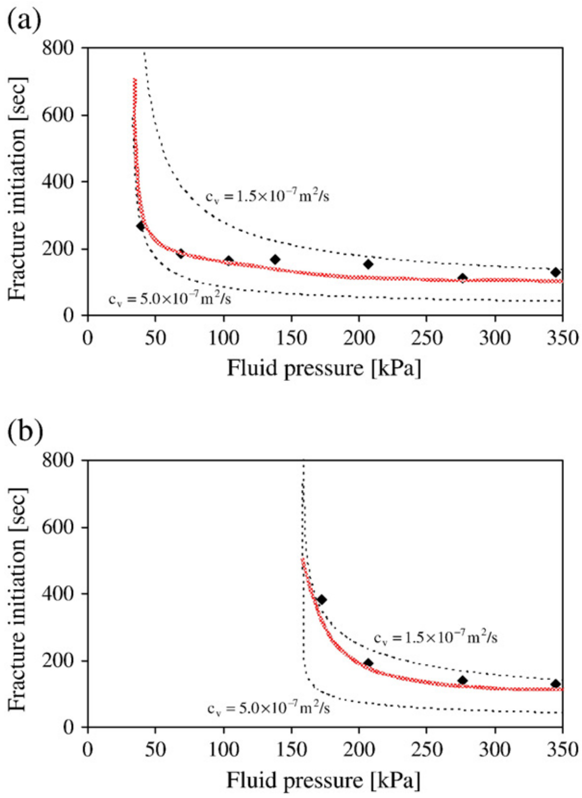

Fig. 7. Fracture initiation time versus applied pressure—Prediction and observations. Observed and estimated fracture initiation time using measured interval value of diffusion coefficient $c_v = 1.5 \sim 5.0 \times 10^{-7}$ m^2/s for (a) immiscible fluid for $\rho T_s S_s / 10^{\alpha\sigma^*} = 75$ kPa where specific surface $S_s = 300$ m^2/g for the sediment in this study by Methylene blue absorption method (Santamarina et al., 2002), (b) estimated miscible fluid for $i_c = 7 \times 10^3$.

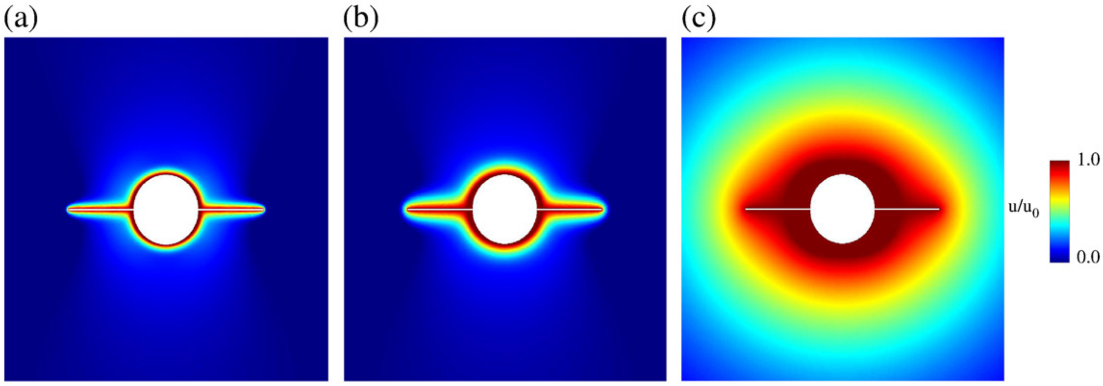

Fig. 8. Fluid pressure distribution around the borehole with existing open fracture during pressure diffusion (a) $T_v = 10^{-4}$, (b) $T_v = 5 \times 10^{-4}$, and (c) $T_v = 0.12$. The simulation parameters are applied fluid pressure in the borehole $u_0 = 200$ kPa, effective confining pressure $\sigma_0 = 100$ kPa, and intact hydraulic conductivity $k = 1.0 \times 10^{-6}$ m/s.

horizontal hydraulic gradient i_C to form an opening-mode fracture, e.g. stiffer media require a higher hydraulic gradient. In terms of the transverse tensile strain ε_x, we can anticipate:

$$\varepsilon_x = \frac{i_C}{E}\sqrt{\gamma_f k \mu}. \tag{7}$$

The relative roles of fluid viscosity μ, sediment stiffness E and hydraulic conductivity k are readily seen in this expression. The predicted fracture initiation times computed for the inverted/estimated critical hydraulic gradient i_C are plotted together with experimental observations in Figure 7b. The relationship between fracture initiation time and applied pressure u_{inv} shows a trend similar to the case of immiscible fluid invasion: infinite initiation time at low u_{inv} (i.e., no hydraulic fracture) and asymptotically shorter time at high u_{inv}.

5.3.3. Comparison

The effective stress fields in the vicinity of defects are different in the two cases. Consequently, fracture pressure with miscible fluids is higher than that with immiscible fluids, as shown in Figure 7.

5.4. Borehole geometry

The most common situation for hydraulic fractures is around boreholes. Let us explore this case within the framework of hydraulic fracture mechanisms identified above.

5.4.1. Immiscible fluid

The borehole experiences axi-symmetric cavity expansion during the early stages of pressurization. The maximum pressure difference

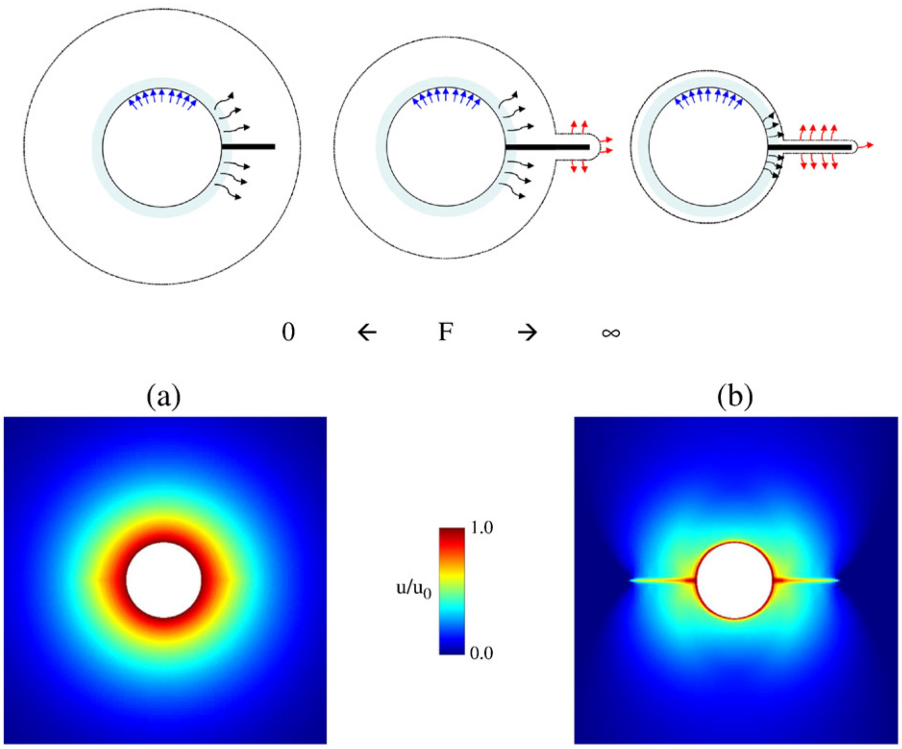

Fig. 9. Effect of dimensionless F on the hydraulic fracture propagation with miscible fluid. (a) Low $F = t_{diff}/t_{frac}$ for no propagation-closed, intermediate F for trapped propagation, and high F for propagation. (b) Finite element analysis for fracture propagation with miscible fluid. Propagation of fluid pressure along the horizontal direction: case with $u_0 = 200$ kPa, $k = 1.0 \times 10^{-3}$ m/s (Left), case with $u_0 = 200$ kPa, $k = 5.0 \times 10^{-9}$ m/s (Right) for confining pressure 100 kPa.

at fracture initiation P_{max} decreases as the tangential extensional strain ε_θ (positive for tensile deformation) around the borehole increases. Then Eq. (4) becomes:

$$P_{\max} = \frac{\rho T_S S_S}{e(1+\varepsilon_\theta)} \frac{1}{10^{\alpha\sigma*}}. \tag{8}$$

Cavity expansion continues until the borehole pressure reaches P_{max} and a fracture initiates. Lower sediment stiffness increases the tangential tensile strain around the borehole and lowers the fracture initiation pressure. Stress-dependent sediment stiffness $E(\sigma')$ and void ratio $e(\sigma')$ combine in Eq. (8) to produce a fracture pressure ratio P_{max}/σ_j' that is higher in shallower bore holes, in agreement with experimental observations (Bohloli and de Pater, 2006).

5.4.2. Miscible fluid

There is early borehole expansion driven by the seepage force. Once a fracture is initiated, fast fracture propagation can be sustained at lower fracture pressure because short times prevent the diffusive homogenization of the fluid pressure field, as shown in Figure 8. The time for pressure diffusion can be estimated as $t_{diff}=L^2/c_v$, and the time for fracture propagation as $t_{frac}=L/V_{frac}$. The fracture propagation velocity V_{frac} is inferred from the Perkins-Kern-Nordgren PKN model under a large fluid leak-off condition and previous experimental observations with uncemented soils (Atkinson et al., 1994; de Pater et al., 1994; Nordgren, 1972)

$$V_{frac} \propto \frac{1}{\gamma\sqrt{E\mu}} \frac{\left(u_0-\sigma_0'\right)^2}{\sqrt{t}}. \tag{9}$$

The dimensionless ratio τ between the two time scales becomes

$$\tau = \frac{t_{diff}}{t_{frac}} \propto \frac{\left(u_{inv}-\sigma_0'\right)^4/\left(\gamma^2 E\mu\right)}{c_v} = \frac{\left(u_{inv}-\sigma_0'\right)^4}{k} \frac{1}{\gamma\mu E^2}. \tag{10}$$

This ratio provides the relationship between governing parameters: sediment stiffness E or compressibility $m_v(\propto 1/E)$, fluid pressure diffusion coefficient $c_v=k/(\gamma m_v)$, borehole pressure u_{inv} and effective confining stress σ_0'. Note that pressure diffusive homogenization requires increasingly more time in fractures away from the borehole and lower fluid pressure could be needed for fracture growth. However, viscous drag along the fracture plane has the opposite effect on the required borehole pressure.

Low τ-values imply that radial pressure diffusion is faster than fracture propagation in this case, there is low hydraulic gradient normal to the fracture direction, fractures do not propagate, and pre existing fractures close (Fig. 9a). The converse is true at high τ-values, where high hydraulic gradients normal to the fracture surface produce large drag forces and facilitate further fracture propagation at the tip. Numerical results (shown in Fig. 9b) confirm these predictions.

The approximate relationship between the applied fluid pressure u_{inv} and the confining effective stress σ_0' is given by $(u_{inv}-\sigma_0')\propto\sqrt[4]{k}\sqrt{\sigma_0'}$ suggesting that high leak-off in high hydraulic conductivity sediments will require higher fracture pressure. The increase in u_{inv}/σ_0' with decreasing σ_0' implies relatively higher fracture formation in shallow boreholes (Alfaro and Wong, 2001; Pruiksma and Bezuijen, 2002), this is analogous to the immiscible fluid case.

6. Conclusions

Fluid-driven hydraulic fracture initiation and propagation in uncemented granular materials have been explained either as tensile failure or shear failure, in part due to apparent similarities with fracture patterns in solid materials. However, these hypotheses contradict the inherent effective stress frictional behavior of cohesionless granular materials and fail to justify experimental observations. Experiments, particle-scale analyses and macro-scale simulation results obtained in this study provide unprecedented insight into hydraulic fracture initiation and growth in granular materials.

Distinct particle-level mechanisms develop whether the invading fluid is miscible or immiscible with the host fluid. Weight and skeletal forces decrease faster than capillary and drag forces with decreasing particle size; hence, fine-grained soils are more susceptible to fluid-driven fracture formation.

Increased porosity at the fracture tip and strains preferentially normal to the fracture alignment are common to both miscible and immiscible fluid-driven fractures. Then, a self-feeding sequence of events sustains fracture initiation and growth: increased porosity at the tip, eased interfacial membrane invasion or pronounced increase in longitudinal hydraulic conductivity, development of capillary or seepage forces that promote fracture opening, increased porosity at the new tip location.

These mechanisms can be used to explain the following experimental observations: (1) longer fracture initiation time when the imposed pressure is low in diffusion-controlled systems; (2) the relevance of surface defects on fracture nucleation and their secondary effect on the required fracture pressure; (3) the role of defect geometry on early propagating direction; (4) the higher ratio between fracture pressure and effective confining stress at shallow depth; (5) lower initiation pressure in boreholes than on planar surfaces; and (6) reduced fluid pressure diffusion and homogenization when high propagation velocity is imposed with miscible fluids, resulting in more efficient fracture propagation.

Acknowledgements

Support for this research was provided by the Goizueta Foundation, the National Science Foundation, and the U.S. Depart of Energy. We would like to thank M. Dusseault for introducing us to the scientific challenges posed by hydraulic fractures in sediments. We are also grateful to L. Germanovich for enlightening discussions and to A. Sivaram for proof-reading the manuscript.

Appendix A. Supplementary data

Supplementary data to this article can be found online at doi:10.1016/j.epsl.2010.08.033.

References

Alfaro, M.C., Wong, R.C.K., 2001. Laboratory studies on fracturing of low-permeability soils. Can. Geotech. J. 38 (2), 303–315.
Andersen, K.H., Rawlings, C.G., Lunne, T.A., By, T.H., 1994. Estimation of hydraulic fracture pressure in clay. Can. Geotech. J. 31 (6), 817–828.
Ang, A.H.S., Tang, W.H., 1975. Probability Concepts in Engineering Planning and Design, 1. John Wiley, New York.
Atkinson, J.H., Charles, J.A., Mhach, H.K., 1994. Undrained hydraulic fracture in cavity expansion tests. Proceedings of the 13th International Conference on Soil Mechanics and Foundation Engineering, 3. A.A. Balkema, New Delhi, India, pp. 1009–1012.
Bardet, J.P., 1997. Experimental Soil Mechanics. Prentice Hall, Upper Saddle River, N.J.
Bai, T., Pollard, D.D., Gao, R., 2000. Explanation for fracture spacing in layered materials. Nature 403 (6771), 753–756.
Bjerrum, L., Kennard, R.M., Gibson, R.E., Nash, J., 1972. Hydraulic fracturing in field permeability testing. Geotechnique 22 (2), 319–332.
Bohloli, B., de Pater, C.J., 2006. Experimental study on hydraulic fracturing of soft rocks: influence of fluid rheology and confining stress. J. Pet. Sci. Eng. 53 (1–2), 1–12.
Brown, K.M., Bekins, B., Clennell, B., Dewhurst, D., Westbrook, G., 1994. Heterogeneous hydrofracture development and accretionary fault dynamics. Geology 22 (3), 259–262.
Cailly, B., Le Thiez, P., Egermann, P., Audibert, A., Vidal-Gilbert, S., Longaygue, X., 2005. Geological storage of CO_2: a state-of-the-art of injection processes and technologies. Oil Gas Sci. Technol. 60 (3), 517–525.

Chalbaud, C., Robin, M., Lombard, J.M., Martin, F., Egermann, P., Bertin, H., 2009. Interfacial tension measurements and wettability evaluation for geological CO_2 storage. Adv. Water Res. 32 (1), 98–109.

Chang, H., 2004. Hydraulic fracturing in particulate materials, Georgia Institute of Technology. Ph.D thesis.

Debschutz, W., Kruckel, U., Schopper, J.R., 1989. Effect of Geostatic Stress and Pore Pressure on the Klinkenberg Permeability Factor and other Fluid Flow Parameter. In: Maury, V., Fourmaintraux, D. (Eds.), Proc. Symp. Rock at Great Depth, Balkema, Rotterdam, pp. 79–186.

de Pater, C.J., Cleary, M.P., Quinn, T.S., Barr, D.T., Johnson, D.E., Weijers, L., 1994. Experimental verification of dimensional analysis for hydraulic fracturing. SPE Prod. Facil. 9 (4), 230–238.

de Pater, C.J., Dong, Y., 2007. Experimental study of hydraulic fracturing in sand as a function of stress and fluid rheology. SPE—Hydraulic Fracturing Technology Conference 2007 2007. Society of Petroleum Engineers, College Station, TX, United States, pp. 87–96.

Economides, M.J., Nolte, K.G., 2000. Reservoir Stimulation. Wiley, Chichester, England.

Garcia-Bengochea, I., Lovell, C.W., Altschaeffl, A.G., 1979. Pore distribution and permeability of silty clays. J. Geotech. Eng. Div. 105 (7), 839–856.

Hubbert, M.K., Willis, D.G., 1957. Mechanics of hydraulic fracturing. Trans. Am Inst. Min. Metall. Eng. 210 (6), 153–163.

Jaky, J., 1944. The coefficient of earth pressure at rest. J. Union Hung. Eng. Archit. 355–358.

Jaworski, G.W., Duncan, J.M., Seed, H.B., 1981. Laboratory study of hydraulic fracturing. J. Geotech. Eng. Div. 107 (6), 713–732.

Juang, C.H., Holtz, R.D., 1986. Fabric pore size distribution and permeability of sandy soils. J. Geotech. Eng. 112 (9), 855–868.

Keck, R.G., Withers, R.J., 1994. Field demonstration of hydraulic fracturing for solids waste injection with real-time passive seismic monitoring. Proceedings—SPE Annual Technical Conference and Exhibition Pi. Society of Petroleum Engineers (SPE), New Orleans, LA, USA, pp. 319–334.

Khodaverdian, M., McElfresh, P., 2000. Hydraulic fracturing stimulation in poorly consolidated sand: Mechanisms and consequences. SPE Reservoir Engineering. Society of Petroleum Engineers (SPE), Dallas, TX, United states, pp. 715–727.

Komak Panah, A., Yanagisawa, E., 1989. Laboratory studies on hydraulic fracturing criteria in soil. Soils Found. 29 (4), 14–22.

Leonards, G.A., Davidson, L.W., 1984. Reconsideration of failure initiating mechanisms for Teton dam. First International Conference on Case Histories in Geotechnical Engineering 3, pp. 1103–1113. St. Louis, Mo.

Li, X., Zhang, L.M., 2009. Characterization of dual-structure pore-size distribution of soil. Can. Geotech. J. 46 (2), 129–141.

Mori, A., Tamura, M., 1987. Hydrofracturing pressure of cohesive soils. Soils Found. 27 (1), 12–24.

Muir Wood, D., 1990. Soil Behaviour and Critical State Soil Mechanics. Cambridge University Press, Cambridge, England.

Murray, R.S., Quirk, J.P., 1990. Intrinsic failure and cracking of clay. Soil Sci. Soc. Am. J. 54 (4), 1179–1184.

Nemat-Nasser, S., Abe, H., Hirakawa, S., 1982. Hydraulic Fracturing and Geothermal Energy. M. Nijhoff Publishers.

Nordgren, R.P., 1972. Propagation of a vertical hydraulic fracture. SPE J. 12 (8), 306–314.

Palomino, A.M., Santamarina, J.C., 2005. Fabric map for kaolinite: effects of pH and ionic concentration on behavior. Clays Clay Miner. 53 (3), 211–223.

Pruiksma, J.P., Bezuijen, A., 2002. Hydraulic fracturing with distinct element method—PFC2D simulations. GeoDelft 151.

Rice, J.R., 1992. Fault Stress States, Pore Pressure Distributions, and the Weakness of the San Andreas Fault. In: Evans, B., Wong, T.F. (Eds.), Fault Mechanics and Transport Properties of Rocks. Academic Press, pp. 475–503.

Schofield, A.N., 1980. Cambridge geotechnical centrifuge operations. Geotechnique 30 (3), 227–268.

Sherard, J.L., 1986. Hydraulic fracturing in embankment dams. J. Geotech. Eng. 112 (10), 905–927.

Shi, Y., Wang, C.Y., 1986. Pore pressure generation in sedimentary basins: overloading versus aquathermal. J. Geophys. Res. 91, 2153–2162.

Soga, K., Gafar, K.O., Ng, M.Y.A., Au, S.K.A., 2006. Macro and micro behaviour of soil fracturing. Proceedings of the International Symposium on Geomechanics and Geotechnics of Particulate Media. Taylor and Francis/Balkema, Ube, Yamaguchi, Japan, pp. 421–427.

Stewart, M.L., Ward, A.L., Rector, D.R., 2006. A study of pore geometry effects on anisotropy in hydraulic permeability using the lattice-Boltzmann method. Adv. Water Res. 29, 1328–1340.

Tanaka, H., Shiwakoti, D.R., Omukai, N., Rito, F., Locat, J., Tanaka, M., 2003. Pore size distribution of clayey soils measured by mercury intrusion porosimetry and its relation to hydraulic conductivity. Soils Found. 43 (6), 63–73.

Terzaghi, K., Peck, R.B., Mesri, G., 1996. Soil Mechanics in Engineering Practices. Wiley, New York.

Toshikazu, H., Yoshiyuki, M., Kenichi, M., Shigeyasu, A., 2002. Features of crack propagation by hydraulic fracturing in cohesive soil. Experimental study on seepage failure of small earth dams. Transactions of the Japanese Society of Irrigation. Drain. Reclam. Eng. 219, 383–392.

Towner, G.D., 1988. The influence of sand- and silt-size particles on the cracking during drying of small clay-dominated aggregates. J. Soil Sci. 39 (3), 347–356.

Wang, Y.H., Xu, D., 2007. Dual porosity and secondary consolidation. J. Geotech. Geoenviron. Eng. 133 (7), 793–801.

Weinberger, R., 1999. Initiation and growth of cracks during desiccation of stratified muddy sediments. J. Struct. Geol. 21 (4), 379–386.

Widjaja, H., Duncan, J.M., Seed, H.B., 1984. Scale and time effects in hydraulic fracturing. US Army Corps of Engineers, Vicksburg. p. 192.

Wong, R.C.K., 2003. A model for strain-induced permeability anisotropy in deformable granular media. Can. Geotech. J. 40, 95–106.

Yanagisawa, E., Panah, A.K., 1994. Two dimensional study of hydraulic fracturing criteria in cohesive soils. Soils Found. 34 (1), 1–9.

Zabat, M., Vayer-Besançon, M., Harba, R., Bonnamy, S., Van Damme, H., 1997. Surface Topography and Mechanical Properties of Smectite Films. Springer, Berlin/Heidelberg.